Contents lists available at SciOpen

Food Science and Human Wellness

journal homepage: https://www.sciopen.com/journal/2097-0765

China Food Publishing Co.

Biosensing analysis based on Au-Cu bimetallic nanoclusters for colorimetric and fluorescent detection of aflatoxin B_1 in cereals and milk

Hui Deng[a,b,c,1], Songlin Liu[a,b,c,1], Xin Deng[a,b,c], Xu Wang[d,e], Ying Xiong[a,b,c], Qian Wen[a,b,c], Wang Li[a,b,c], Yanni Chen[a,b,c,*], Jiali Ren[a,b,c,*]

[a]College of Food Science and Engineering, Central South University of Forestry and Technology, Changsha 410004, China
[b]National Engineering Research Center of Rice and Byproduct Deep Processing, Central South University of Forestry and Technology, Changsha 410004, China
[c]Hunan Key Laboratory of Forestry Edible Sources Safety and Processing, Central South University of Forestry and Technology, Changsha 410004, China
[d]Institute of Quality Standard and Monitoring Technology for Agro-products of Guangdong Academy of Agricultural Sciences, Guangzhou 510640, China
[e]Key Laboratory of Testing and Evaluation for Agro-product Safety and Quality, Ministry of Agriculture and Rural Affairs, Guangzhou 510640, China

ARTICLE INFO

Article history:
Received 9 June 2024
Received in revised form 1 July 2024
Accepted 22 July 2024

Keywords:
Aflatoxin B_1
Dual-mode
Bimetallic nanoclusters
Oxidase-like activity

ABSTRACT

Aflatoxin B_1 (AFB_1) in food is a threaten to food safety and human health. In this study, a colorimetric and fluorescent dual-mode aptamer sensor was constructed for rapid and accurate detection of AFB_1 based on polyvinylpyrrolidone-gold-copper bimetallic nanoclusters (PVP-Au/CuNCs) and Mn_3O_4 nanoparticles (Mn_3O_4 NPs). In the presence of AFB_1, the AFB_1 aptamer on the surface of Mn_3O_4 NPs specifically bound to AFB_1. The oxidase-like activity of Mn_3O_4 NPs was restored and 3,3′,5,5′-0tetramethylbenzidine (TMB) was oxidized to oxidized TMB (oxTMB), which quenched the orange fluorescence of the PVP-Au/CuNCs. With AFB_1 concentrations increasing, the blue color of oxTMB deepened, the fluorescence quenching efficiency was enhanced. The working range was 0–56 μg/L with a limit of detection (LOD) of 0.36 μg/L (colorimetric), and 2.86–40.00 μg/L with a LOD of 0.29 μg/L (fluorescent). In addition, the established sensor was successfully applied to determine AFB_1 in milk, rice, oats, and corn, with a recovery rate of 91.1%–107.5%. This study provides an insight for fabricating a sensitive, efficient, and accurate analytical platform for rapid detection of AFB_1 in food.

1. Introduction

Aflatoxins (AFs) are predominant mycotoxins, accounting for nearly 93% of mycotoxin contamination in foods and beverages[1]. AFs are dihydrofuranocoumarin derivatives with similar chemical structures. AFs include aflatoxins B_1 (AFB_1), B_2 (AFB_2), G_1 (AFG_1), G_2 (AFG_2), and M_1 (AFM_1), which are secondary metabolites produced mainly by *Aspergillus flavus* and *Aspergillus parasiticus*[2]. AFB_1 is considered as the most toxic due to its carcinogenic, teratogenic, and mutagenic nature[3-4]. AFB_1 has been designated as a Class I chemical carcinogen for humans by the International Agency for Research on Cancer (IARC)[5]. Many countries and organizations have regulated the maximum residue limit (MRL) of AFB_1 in food to prevent humans and animals from ingesting excessive AFB_1. In European Union, the MRL of AFB_1 in rice is set at 5 μg/kg, and in peanuts, nuts, dried fruits, and grains are set at 2 μg/kg[6]. In addition, China has implemented an MRL of 20 μg/kg for AFB_1 in corn and related products for human consumption, an MRL of 5 μg/kg for AFB_1 in wheat, barley, and other cereals[7], and an MRL of 5 μg/kg for AFB_1 in milk[8].

Various analytical methods have been developed to detect AFB_1 in food. Traditional analytical methods based on instruments include

[1] These authors contributed equally to this work and should be regarded as co-first authors.
[*] Corresponding authors at: College of Food Science and Engineering, Central South University of Forestry and Technology, Changsha 410004, China.
E-mail address: ynchen@csuft.edu.cn (Y.N. Chen); jialiren_zhen@hotmail.com (J.L. Ren)
Peer review under responsibility of Beijing Academy of Food Sciences.

SciOpen Publishing services by Tsinghua University Press

http://doi.org/10.26599/FSHW.2024.9250363

high-performance liquid chromatography[9], liquid chromatography-mass spectrometry[10], and thin-layer chromatography are accurate and sensitive[11-12]. However, these instrumental methods have disadvantages of expensive instruments, labor-intensive work, and cumbersome samples pretreatment[13]. Therefore, rapid and sensitive detection methods are needed for the fast and high-throughput quantitative analysis of AFB_1[14].

Metal nanoclusters (MNCs) usually consist of several to hundreds of atoms and exhibit specific molecular properties[15–17]. Among these, copper nanoclusters (CuNCs) are easily obtainable, inexpensive, and possess the unique property of aggregation-induced emissions (AIE). CuNCs have the advantages of low toxicity, favorable biocompatibility, a long Stokes shift, and facile synthesis[18], making them suitable fluorescent probes for biosensing and bioimaging[19]. Previous studies reported that most CuNCs were prone to oxidation in air, which adversely affected their fluorescence emission intensity[20]. These limitations of CuNCs hinder their widespread application in biosensing. Compared with single MNCs, bimetallic nanoclusters possessed more excellent catalytic activity and stronger luminescence properties[21-22]. Wang et al.[23] successfully encapsulated Ag-doped Au nanoclusters (Ag/AuNCs) in a ZIF-8 framework to construct a novel Ag/AuNCs@ZIF-8 ratio fluorescent probe for the detection of antibiotic doxycycline (DOX) with a detection limit of 36.8 μg/L. He et al.[24] used aptamers to bridge Fe_3O_4@Au nanoflowers and Au@Ag nanospheres for ultrasensitive SERS to detect AFB_1. Liu et al.[25] developed a novel fluorescent gold/silver nanocluster (Au/Ag NCs) with the help of chondroitin sulfate and realized sensitive detection of hyaluronidase (HAase). Bimetallic nanoclusters based on colorimetric/fluorescent[26] serves as a promising candidate to develop new approaches in field detection[27].

In recent years, nanozymes have been widely used in biosensing due to their excellent enzyme-like catalytic activity. Nanozymes have garnered significant attention as alternatives to natural enzymes. They have numerous advantages, such as high stability, low cost, easy synthesis, and tunable properties[28], which make them highly attractive in biosensing[29]. Numerous nanozymes have been synthesized and employed as probes for the detection of various analytes[30-31]. The Mn_3O_4 NPs are easily synthesized, surface-modified, and exhibit diverse enzyme-mimetic activities, including oxidase, superoxide dismutase, and catalase activities. The Mn_3O_4 NPs readily interact with biomolecules, such as aptamers, through hydrogen bonding, van der Waals forces, electrostatic interactions, and coordinate bonds, resulting in a tremendous potential for constructing nanozyme-based biosensors[32-33]. Aptamers, known for their exceptional affinity, stability, and specificity[34], have been widely employed as crucial components of biosensors[35]. In addition, negatively charged aptamers regulate the interfacial properties of nanozymes through modulating the nanozyme activity[36].

In this study, a bimodal colorimetric and fluorescent biosensor based on multifunctional PVP-Au/CuNCs as fluorescent probes and Mn_3O_4 NPs as nanoenzymatic materials was developed. Mn_3O_4 NPs catalyzed the oxidation of colorless 3,3',5,5'-tetramethylbenzidine (TMB) into blue oxTMB, quenching the fluorescence of PVP-Au/CuNCs. Simultaneously, the aptamer inhibited the oxidase-like activity of Mn_3O_4 NPs, thereby affecting the generation of oxTMB. In contrast, in the presence of AFB_1, it preferentially bound to the aptamer, restoring oxidase-like activity and decreasing fluorescence intensity. The dual-mode biosensor rapidly and accurately detected AFB_1 based on these phenomena.

2. Materials and methods

2.1 Materials and apparatus

AFB_1, patulin (PAT), ochratoxin A (OTA), trichothecenes (T-2), AFM_1 and zearalenone (ZEN) were purchased from Tanmo Quality Inspection-Standard Material Center. Ethylene glycol (PEG200). Polyvinylpyrrolidone (PVP), copper chloride dihydrate ($CuCl_2{\cdot}2H_2O$), magnesium chloride ($MgCl_2$), 2-mercaptobenzothiazole (MBT), TMB, trifluoroacetic acid (TFA), and methanol were purchased from Shanghai McLean Biochemical Technology Co., Ltd. Sodium hydroxide and sodium chloride were purchased from Sinopharm Chemical Reagent Co.,Ltd. AFB_1 aptamer[37] (5′-GTTGGGCACGTGT TGTCTCTCTGTGTCTCGTGCCCTTCGCTAGGCCCACA-3′), poly A (5′-AAAAAAAAAAAA-3′), poly T (5′-TTTTTTTTTTTT-3′), poly G (5′-GGGGGGGGGGGG-3′) and poly C (5′-CCCCCCCCCCCC-3′) were obtained from Shanghai Sangon Biotech Co., Ltd. Chemical reagents used in this experiment were at least analytical grade, and water used throughout the experiment was ultrapure.

Morphology of PVP-Au/CuNCs and Mn_3O_4 NPs were characterized by a JEM-F200 high-resolution transmission electron microscope (TEM) (JEOL, Japan). Fluorescence spectra were obtained on a G9800A fluorescence spectrophotometer (Agilent, USA). UV-visible absorption spectra were recorded on a UV-2600 UV spectrophotometer (Shimadzu, Japan).

2.2 Synthesis of PVP-Au/CuNCs

First, the PVP-Au/CuNCs were synthesized using one-pot method[38]. Briefly, 5 mL PVP (1.0 mmol/L), 2 mL MBT (10.0 mmol/L), 1 mL $HAuCl_4$ (2.5 mmol/L), 3 mL SC (2.5 mmol/L), and 2 mL of $CuCl_2{\cdot}2H_2O$ (2.5 mmol/L) were sequentially added to the vessel. The mixture was stirred for 1 h in the dark at 25 °C. The resulting light-yellow solution was dialyzed for 24 h. The final solution was stored in the dark at 4 °C for use. Fluorescence spectra were collected using a fluorescence spectrometer, and the fluorescence lifetime was obtained using steady-state/transient fluorescence spectrometer scanning. The average fluorescence lifetime was calculated using the equation:

$$\tau_{average} = \frac{A_1\tau_1^2 + A_2\tau_2^2}{A_1\tau_1 + A_2\tau_2} \quad (1)$$

Where τ_1 and τ_2 represent the attenuation time constants under different radiation attenuation; A_1 and A_2 represent the corresponding amplitudes, respectively.

2.3 Synthesis of Mn_3O_4 NPs

Mn_3O_4 NPs were synthesized using a hydrothermal method[39]. In brief, 87.5 mg $KMnO_4$ was dissolved in ultrapure water (25 mL), followed by the addition of 25 mL of PEG-200. Subsequently, the mixed solution was stirred at 25 °C for 30 min until its color changed from dark purple to dark brown. The mixed solution was transferred into a stainless steel autoclave lined with polytetrafluoroethylene and then heated at 120 °C for 8 h. The resulting brown precipitates were collected by centrifugation at 10 000 r/min for 5 min and alternately washed with water and ethanol several times. Purified Mn_3O_4 NPs were dried at 40 °C for 12 h and stored at 25 °C for use.

2.4 Enzyme kinetics experiments of octahedral Mn_3O_4 NPs

Owing to the excellent oxidase-like activity of Mn_3O_4 NPs, the Michaelis-Menten (K_m) constant and maximum reaction rate (V_{max}) were determined. A steady-state kinetic analysis of the octahedral Mn_3O_4 NPs was performed using TMB as the substrate. The concentration of Mn_3O_4 NPs was maintained constant, whereas that of TMB ranged from 0.2 to 1.4 mmol/L. The absorbance at 652 nm was recorded every 90 s. K_m and V_{max} were calculated using the linear Weaver-Burk equation (2) and (3):

$$V = \frac{V_{max}[S]}{K_m + [S]} \tag{2}$$

$$\frac{1}{V} = \frac{K_m}{V_{max}[S]} + \frac{1}{V_{max}} \tag{3}$$

Where V represents the initial rate, V_{max} is the maximum reaction rate, K_m is the Michaelis constant, and [S] is the substrate concentration.

2.5 Establishment of dual-mode

First, the aptamer solution was heated at 95 °C for 5 min and then annealed at 25 °C to form a stable spatial structure. Then, 20 μL of Mn_3O_4 NPs solution and 20 μL of AFB_1 aptamer solution (150 nmol/L) were mixed thoroughly and incubated at 25 °C for 10 min. Subsequently, 20 μL of AFB_1 standard solution was added to the above mixture and incubated at 37 °C for 30 min. Then, an appropriate volume of sodium acetate buffer (20 mmol/L, pH 3.5) and 20 μL of TMB (10 mmol/L) were added to the reaction mixture, which was incubated at 30 °C for 20 min. The absorbance was recorded using a UV-visible spectrophotometer from 500 to 800 nm. The absorbances at 652 nm for the target sample (A) and the blank sample (A_0) were recorded. All samples were tested in triplicates. The change in the relative absorbance value ($(A - A_0)/A_0$) was calculated to evaluate the colorimetric detection of AFB_1 using an aptamer sensor. Finally, a working curve was plotted with the AFB_1 concentration as the horizontal coordinate and $(A - A_0)/A_0$ as the vertical coordinate.

A total of 150 μL of PVP-Au/CuNCs was added to the aforementioned colorimetric detection solution. The fluorescence intensity in the 500–800 nm range was measured using a fluorescence spectrophotometer with an excitation wavelength of 360 nm. The fluorescence intensities were recorded before quenching (F_0) and after quenching (F) at 610 nm. All samples were tested in triplicate. The change in the fluorescence quenching rate $(F_0 - F)/F_0$ was calculated to evaluate the fluorescence detection ability of the aptamer sensor for AFB_1. Finally, a working curve was plotted with AFB_1 concentration as the horizontal coordinate and $(F_0 - F)/F_0$ as the vertical coordinate.

2.6 Determination of AFB_1 in actual food samples

The pretreatment of rice, corn, and oat samples was slightly adjusted (Fig. S1) as described in previous research[40]. Briefly, rice, corn, and oat samples were ground into powders. The AFB_1 standard solution was added to the powdered sample (1.0 g). The spiked samples were air-dried naturally. Then, 5 mL of a methanol/water (7:3, V/V) solution was added, followed by continuous ultrasonication and vigorous shaking for 20 min. The mixture was then centrifuged at 10 000 r/min for 15 min, and the resulting supernatant was filtered using a filter membrane (0.22 μm) and stored at 4 °C for further use.

Milk pretreatments were slightly modified (Fig. S2) according to previous research[41]. AFB_1 standard solution was spiked into milk samples. Milk samples were pretreated as follows: 20 mL of milk sample and 1 mL of TFA were mixed. After sonication for 10 min and vortexing for 5 min, the mixture was centrifuged at 10 000 r/min for 20 min to collect the supernatant. The precipitate was extracted twice with 10 mL methanol and centrifugated at 10 000 r/min for 15 min. The supernatants were combined and filtered through a filter membrane (0.22 μm). Subsequently, the pH of the milk filtrate was adjusted to 7.4.

2.7 Statistical analysis

All experiments were performed at least in triplicate. Results were expressed as mean ± standard deviation. The data were applied to one-way analysis of variance and Tukey's test using SPSS software (version 22.0; IBM Co.). P values < 0.05 was considered to be a significant difference.

3. Results and discussion

3.1 Principle of the developed dual-mode sensor

A colorimetric and fluorescent dual-mode sensor based on Mn_3O_4 NPs nanozyme and PVP-Au/CuNCs was developed for the sensitive determination of AFB_1 in food. As depicted in Fig. 1A, PVP-Au/CuNCs with orange fluorescence was synthesized using one-pot method. As shown in Fig. 1B, the negatively charged AFB_1 aptamer was adsorbed on the surface of octahedral Mn_3O_4 NPs through π-π stacking or metal-ligand interactions, enhancing the nagatively charged density. In the absence of AFB_1, Mn_3O_4 NPs with oxidase-like activity was partially inhibited, resulting the degree of oxidation of TMB was decreased, the color of oxTMB showed light blue. In addition, oxTMB with a maximum absorbance at 652 nm and PVP-Au/CuNCs with fluorescence emission at 610 nm realized spectral overlap. The oxTMB quenched orange fluorescence of PVP-Au/CuNCs through the inner filter effect (IFE). There may also be FRET between them due to oxTMB and PVP-Au/CuNCs with opposite charges. In the presence of AFB_1, AFB_1 aptamer on the surface of Mn_3O_4 NPs preferentially bound to AFB_1[2] and detached from the surface of the Mn_3O_4 NPs, Mn_3O_4 NPs significantly oxidized TMB to oxTMB in dark blue. The fluorescence quenching ability of the system was also enhanced with the oxTMB concentrations increasing, and the fluorescence intensity of the PVP-Au/CuNCs at 610 nm was significantly decreased mainly owing to IFE or FRET. Herein, the colorimetric model based on Mn_3O_4 NPs and the fluorescence model based on PVP-Au/CuNCs were successfully established.

3.2 Characterization of PVP-Au/CuNCs and Mn_3O_4 NPs

The morphology of PVP-Au/CuNCs was characterized by transmission electron microscopy (TEM). As shown in Figs. 2A-C, the prepared PVP-Au/CuNCs were uniformly distributed and exhibited a

good crystalline structure with an average size of approximately 2.78 nm (Fig. 2C) and a lattice spacing of approximately 0.214 and 0.240 nm (Fig. 2B), corresponding to the (111) crystal plane of metal Cu (yellow mark)[42] and metal Au (red mark)[43], respectively. The optimal excitation and emission wavelengths of the synthesized PVP-Au/CuNCs were 360 and 610 nm, respectively (Figs. 2D and E), indicating their typical excitation-independent properties. The PVP-Au/CuNCs emitted a strong orange fluorescence under UV irradiation at 375 nm (Fig. 2E), confirming the successful fabrication of PVP-Au/CuNCs. The average lifetime of PVP-Au/CuNCs was 12.45 μs (Fig. 2F).

As shown in Figs. 3A and B, the prepared Mn_3O_4 NPs exhibited octahedral shapes with an average size of approximately 250 nm (Fig. 3C), consistent with previous report. The X-ray diffraction pattern of Mn_3O_4 NPs (Fig. 3D) illustrated that all the measured diffraction peaks matched well with the spinel structure of the Mn_3O_4 NPs ((JCPDS card No. 80-0382) $I4_1/amd$)[44]. Fourier transform infrared spectrum of Mn_3O_4 NPs is shown in Fig. 3E. The vibration band at 416 cm^{-1} is attributed to the vibration of Mn^{3+}–O. The vibration bands at 534 and 641 cm^{-1} were assigned to tetrahedral and octahedral Mn–O stretching vibrations, respectively. The vibration bands at 1 078, 1 151

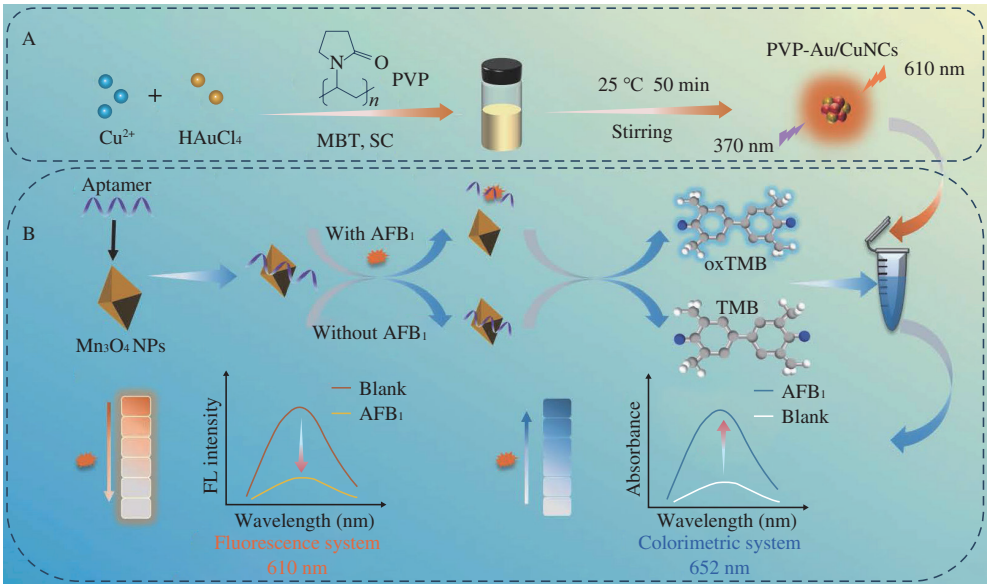

Fig. 1 (A) The synthesis of PVP-Au/CuNCs. (B) The working principle of colorimetric and fluorescent dual-mode sensor for detecting AFB_1.

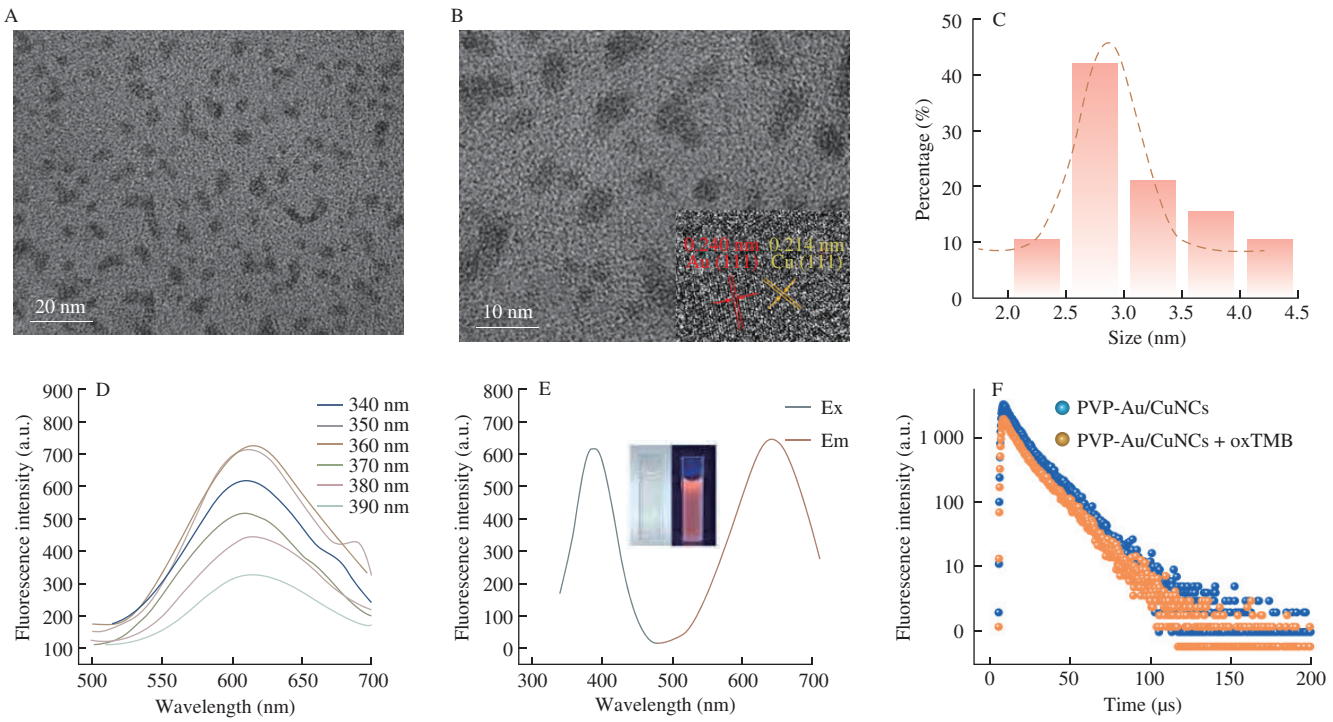

Fig. 2 Characterization analysis of PVP-Au/CuNCs. (A and B) TEM images of PVP-Au/CuNCs; (C) The particle size distribution of PVP-Au/CuNCs; (D) The fluorescence emission of PVP-Au/CuNCs at different excitation wavelengths. (E) The excitation spectrum and emission spectrum of PVP-Au/CuNCs (inset, the solution under fluorescent lamps and irradiation of 375 nm UV lamps). (F) The fluorescence lifetime of PVP-Au/CuNCs.

and 1 625 cm^{-1} were attributed to Mn-OH vibrations[33]. The vibration band at 2 084 cm^{-1} was triggered by the stretching vibration of C=C=C[45]. As shown in Fig. 3F, the Zeta potentials of negatively charged Mn_3O_4 NPs and aptamer were –17.37 and –16.50 mV, respectively, revealing that electrostatic interaction between them was possible and thus could induce FRET. The K_m and V_{max} values of Mn_3O_4 NPs for TMB were calculated according to the Weaver-Burk curve equation (Table S1), indicating the strong affinity and efficient oxidase-like activity of Mn_3O_4 NPs for TMB.

3.3 Feasibility

The detailed mechanisms of the colorimetric and fluorescent modes were shown in Fig. 4A. The aptamer concentration on the surface of Mn_3O_4 NPs regulated the oxidase-like activity of Mn_3O_4 NPs and further regulated the blueness of oxTMB (colorimetric system). The oxTMB quenched orange fluorescence of PVP-Au/CuNCs *via* IFE or FRET (fluorescent system). The overlap between the fluorescence emission spectrum of the PVP Au/CuNCs and the UV absorption spectra of oxTMB, which indicated that IFE triggered fluorescence quenching (Fig. 4B)[46]. The Zeta potential of PVP-Au/CuNCs, oxTMB, and PVP-Au/CuNCs+oxTMB was –4.21, +4.07, and –1.80 mV, respectively. The Zeta potential indicating that oxTMB was adsorbed onto the surface of PVP-Au/CuNCs through electrostatic interactions (Fig. 4C), shortening the distance (≤ 10 nm) of them and inducing FRET.

Mn_3O_4 NPs with oxidase-like activity effectively oxidized TMB to oxTMB (Fig. 4D line a, Table S1). The addition of the aptamer decreased oxidase-like activity of Mn_3O_4 NPs (Fig. 4D line c). In the presence of AFB_1, the oxidase-like activity of Mn_3O_4 NPs recovered owing to specific binding between aptamer and AFB_1 (Fig. 4D line b).

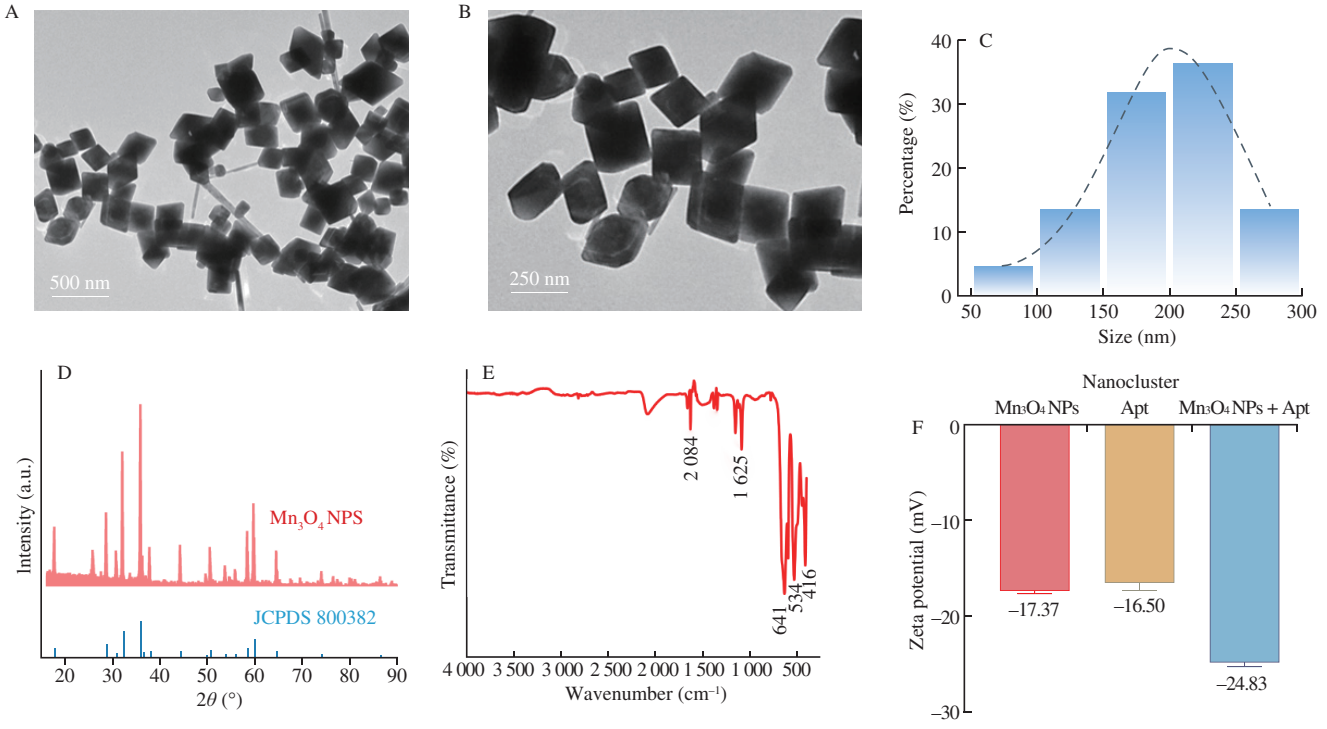

Fig. 3 Characterization analysis of Mn_3O_4 NPs. (A-B) TEM images of Mn_3O_4 NPs; (C) Particle size distribution of Mn_3O_4 NPs; (D) The XRD of Mn_3O_4 NPs; (E) The FT-IR spectrum of Mn_3O_4 NPs; (F) Zeta potential of Mn_3O_4 NPs, aptamer (Apt), and Mn_3O_4 NPs + Apt, respectively.

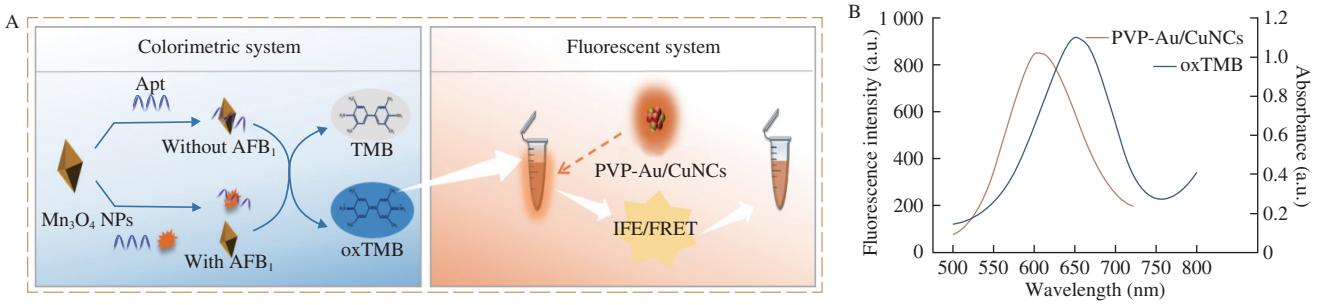

Fig. 4 Feasibility analysis of the developed sensing method. (A) Respective schematic diagrams of the colorimetric and fluorescence modes. (B) The fluorescence spectrum of PVP-Au/CuNCs and the UV visible spectra of oxTMB. (C) The Zeta potential of PVP-Au/CuNCs, oxTMB, and PVP Au/CuNCs + oxTMB, respectively. (D) UV visible spectra of Mn_3O_4 NPs under various conditions (line a: Mn_3O_4 NPs + TMB; line b: Mn_3O_4 NPs + Apt + AFB_1 + TMB; line c: Mn_3O_4 NPs + Apt + TMB; line d: Mn_3O_4 NPs). (E) Fluorescence spectra of PVP-Au/CuNCs under various conditions (line a: PVP-Au/CuNCs; line b: PVP-Au/CuNCs + Mn_3O_4 NPs; line c: Mn_3O_4 NPs + TMB; line d: Mn_3O_4 NPs + Apt + Mn_3O_4 NPs + TMB; line e: Mn_3O_4 NPs + Apt + AFB1 + Mn_3O_4 NPs + TMB; line f: PVP-Au/CuNCs + Mn_3O_4 NPs + TMB).

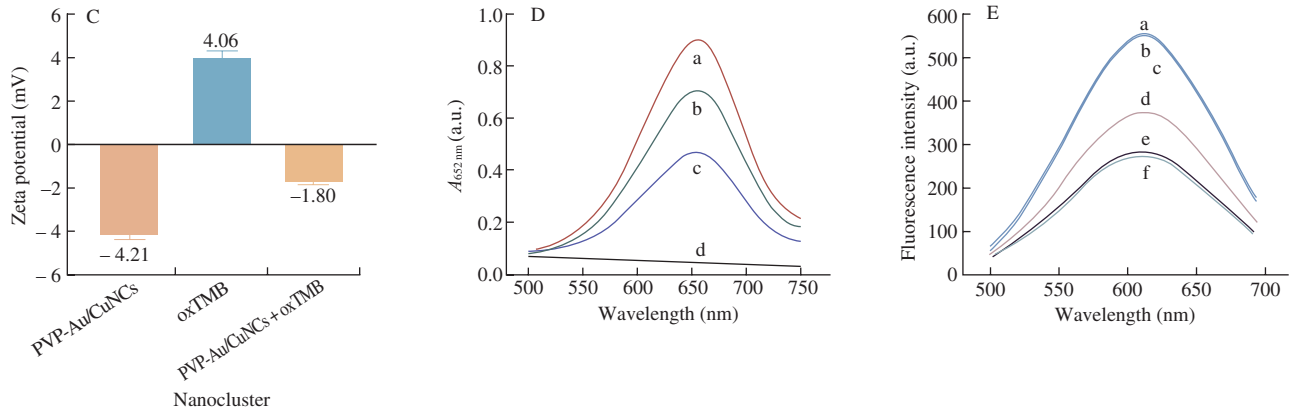

Fig. 4 (*Continued*)

The base G played a crucial role in inhibiting the enzymatic activity of Mn_3O_4 NPs (Fig. S3). As illustrated in Figs. 4E and S4, individual Mn_3O_4 NPs, TMB, AFB_1, aptamer could not influence the orange fluorescence of PVP-Au/CuNCs, the oxTMB significantly quenched the orange fluorescence of PVP-Au/CuNCs (Fig. 4E line f). Mn_3O_4 NPs inhibited by aptamer oxidized partial TMB to form oxTMB and thus quenched the orange fluorescence of PVP-Au/CuNCs (Fig. 4E line d). With AFB_1 aptamer falling off the surface of Mn_3O_4 NPs, the oxTMB gradually increased, the orange fluorescence intensity further decreased (Fig. 4E line e).

3.4 Optimization of experimental conditions

The concentration of Mn_3O_4 NPs was initially optimized. With increasing of Mn_3O_4 NPs concentration, the absorbanc of oxTMB gradually increased (Fig. 5A), the color changed dark blue (Fig. 5A inset). There is a good linear response between absorbance of oxTMB and Mn_3O_4 NPs concentration (Fig. 5B). Considering the cost, synthesis time, and the effect of the resulting oxTMB concentration on the fluorescence intensity of PVP-Au/CuNCs, 20 μg/mL was finally selected for subsequent experiments. To maximize the catalytic activity of the Mn_3O_4 NPs, the reaction pH, temperature, aptamer concentration, and TMB concentration were optimized based on the optimal Mn_3O_4 NP concentration. The relative absorbance $(A–A_0)/A_0$ was calculated to represent the oxTMB concentration, indicating the enzymatic ability of the Mn_3O_4 NPs.

The pH of the reaction system was a crucial factor affecting TMB oxidation. Weakly acidic conditions are generally preferred. This may be because Mn_3O_4 NPs promote dissolved oxygen to produce more hydroxyl radicals in a relatively acidic environment, improving catalytic activity. The enzymatic activity of the Mn_3O_4 NPs was optimal at pH 3.5, which is consistent with previous report (Fig. 5C). The enzymatic activity of Mn_3O_4 NPs gradually enhanced with increasing in reaction temperature (10–50 ℃). The highest relative absorbance at 30 ℃ colorimetric was optimal for colorimetric detection (Fig. 5D). The concentration of aptamer was closely related to the oxidase-like activity of Mn_3O_4 NPs. When the aptamer concentration reached 15 nmol/L, the relative absorbance was optimal, indicating the saturated state of xidase-like activity of the Mn_3O_4 NPs (Fig. 5E). As shown in Fig. 5F, the relative absorbance was maximized when the concentration of TMB reached 1.2 mmol/L.

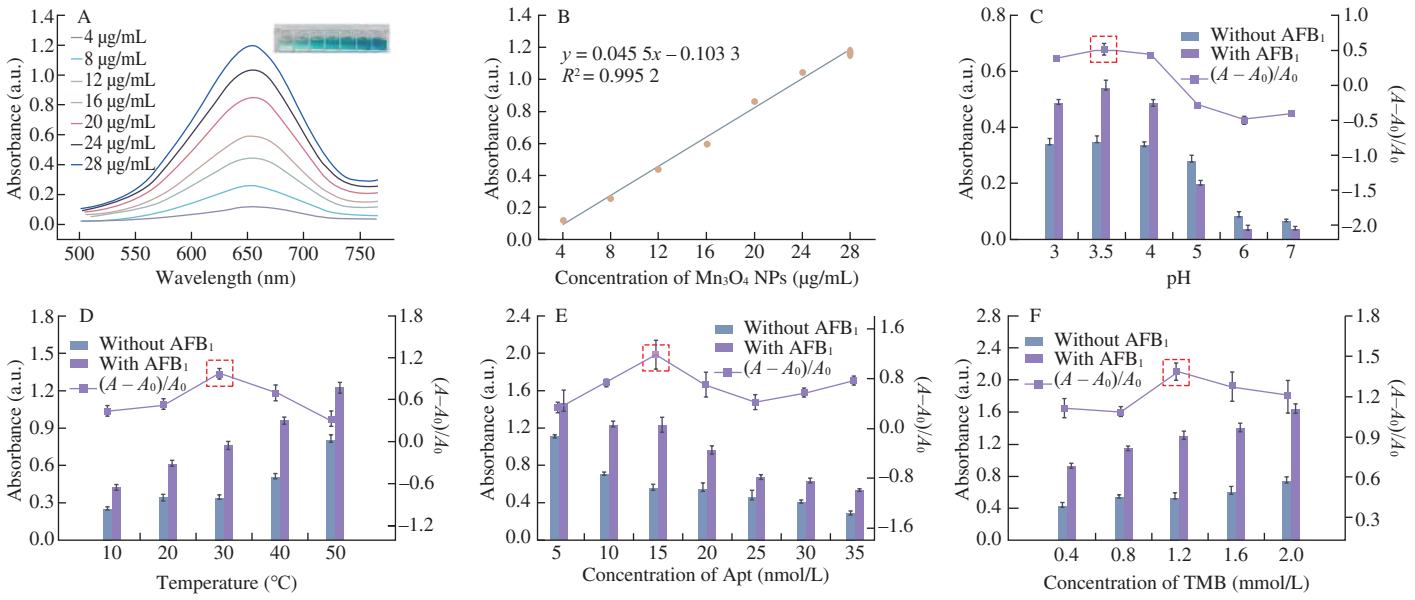

Fig. 5 Optimization of experimental conditions. (A) UV-visible spectra of Mn_3O_4 NPs + TMB at different Mn_3O_4 NPs concentrations; (B) Linear standard curve of Mn_3O_4 NPs concentration and absorbance at 652 nm of Mn_3O_4 NPs + TMB; (C) optimization of pH; (D) optimization of temperature; (E) optimization of aptamer concentration; (F) optimization of TMB concentration. Where A and A_0 are the absorbance at 652 nm in the presence and absence of AFB_1, respectively.

3.5 Sensitivity

The sensitivity of the fabricated colorimetric and fluorescent dual-mode sensor for AFB_1 was evaluated under optimal experimental conditions. As depicted in Fig. 6A, the absorbance in colorimetric mode was positively corelated with AFB_1 concentration in the range of 0–56 μg/L. The linear equation was $y = 0.076\,3\,x + 0.021\,4$ with $R^2 = 0.993\,8$ (Fig. 6B). The LOD of colorimetric mode for AFB_1 was 0.36 μg/L.

In fluorescent mode, with increasing of AFB_1 concentration, the oxTMB concentration increased, the orange fluorescence of PVP-Au/CuNCs was gradually quenched (Fig. 6C). The relative fluorescence intensity showed a good linear relationship with AFB_1 concentration in the range of 2.86–40.00 μg/L. The linear equation was $y = 0.010\,7\,x + 0.057\,7$ with $R^2 = 0.992\,3$ (Fig. 6D). The LOD of fluorescence mode for AFB_1 was 0.29 μg/L. In addition, the performances of several AFB_1 methods recently published.

3.6 Specificity

Five mycotoxins (PAT, OTA, T-2, ZEN, AFM_1) and a mixture of five mycotoxins and AFB_1 were selected to evaluate the specificity of the developed dual-mode sensor. The concentrations of the 5 mycotoxins were more than 10 times the AFB_1 concentration. As shown in Figs. 6E and F, the significant changes in color and fluorescence were observed with the addition of AFB_1 or the mixture. In contrast, no significant changes was observed with the addition of other 5 mycotoxins. The proposed colorimetric and fluorescent dual-mode sensor exhibited remarkable specificity for AFB_1.

Table 1
Spiked-recovery results of the proposed sensor.

Sample	Spiked	Found	Recovery (%)	RSD (%)
Milk	5 μg/L	(5.38 ± 0.48) μg/L	107.54 ± 9.65	7.32
	10 μg/L	(9.24 ± 0.51) μg/L	92.38 ± 5.13	4.53
	20 μg/L	(19.32 ± 0.53) μg/L	96.61 ± 2.65	2.24
Rice	5 μg/kg	(4.59 ± 0.03) μg/kg	91.80 ± 0.62	0.55
	10 μg/kg	(9.98 ± 0.22) μg/kg	99.83 ± 2.23	1.87
	20 μg/kg	(19.82 ± 0.20) μg/kg	99.14 ± 1.01	0.83
Oats	5 μg/kg	(4.96 ± 0.46) μg/kg	99.26 ± 9.15	7.53
	10 μg/kg	(10.11 ± 0.05) μg/kg	101.08 ± 0.47	0.38
	20 μg/kg	(19.52 ± 0.27) μg/kg	97.59 ± 1.36	0.14
Corn	5 μg/kg	(4.75 ± 0.39) μg/kg	94.91 ± 7.78	6.69
	10 μg/kg	(9.11 ± 0.12) μg/kg	91.14 ± 1.17	1.05
	20 μg/kg	(19.50 ± 0.55) μg/kg	97.54 ± 2.74	2.30
Milk	5 μg/L	(5.23 ± 0.39) μg/L	104.76 ± 7.83	7.48
	10 μg/L	(10.40 ± 0.28) μg/L	104.03 ± 2.83	6.10
	20 μg/L	(19.64 ± 1.53) μg/L	98.20 ± 7.69	2.22
Rice	5 μg/kg	(5.13 ± 0.43) μg/kg	102.64 ± 8.73	6.40
	10 μg/kg	(9.74 ± 0.82) μg/kg	97.46 ± 8.28	6.94
	20 μg/kg	(20.34± 0.33) μg/kg	101.71 ± 1.65	6.94
Oats	5 μg/kg	(4.75 ± 0.43) μg/kg	95.18 ± 8.65	7.43
	10 μg/kg	(9.91 ± 0.54) μg/kg	99.14 ± 5.45	4.49
	20 μg/kg	(19.33 ± 0.45) μg/kg	96.65 ± 2.25	1.90
Corn	5 μg/kg	(4.99 ± 0.36) μg/kg	99.89 ± 7.35	6.01
	10 μg/kg	(10.00 ± 0.28) μg/kg	100.06 ± 2.81	2.30
	20 μg/kg	(19.89 ± 0.24) μg/kg	99.49 ± 1.21	1.00

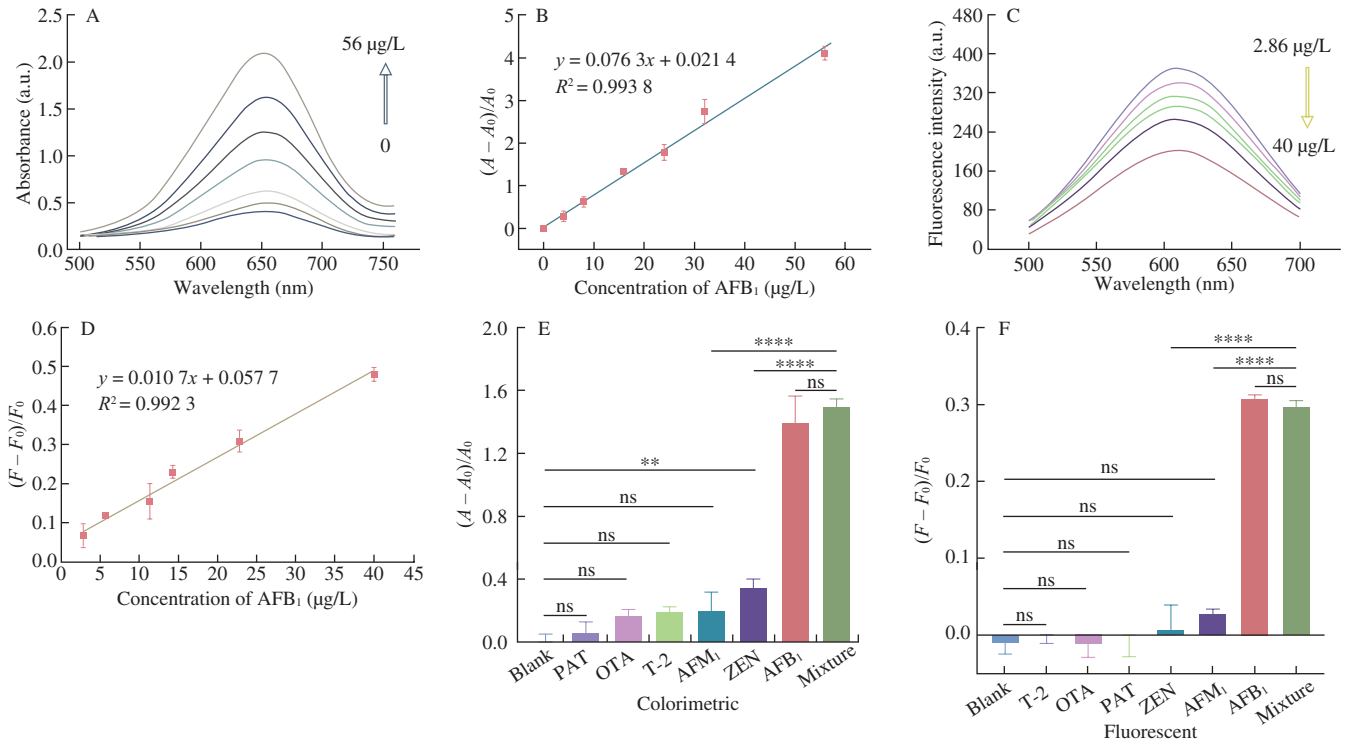

Fig. 6 Sensitivity and specificity of the developed sensor. (A) Absorption spectrum corresponding to various AFB_1 concentrations. (B) Relationship between the relative absorbance value at 652 nm and the concentrations of AFB_1. (C) The fluorescence spectra corresponding to various AFB_1 concentrations. (d) Relationship between the fluorescence quenching rate at 610 nm and the concentrations of AFB_1. where F_0 and F are the fluorescence intensities at 610 nm in the absence and presence of AFB_1, respectively. (E) Specificity of the developed sensor (colorimetric). (F) Specificity of the developed sensor (fluorescent). ns, no significance ($P > 0.05$); *$P < 0.01$, **$P < 0.001$, ****$P < 0.000\ 1$.

3.7 Analysis of AFB_1 in actual food samples

To verify the practicality and reliability of the developed colorimetric and fluorescent dual-mode sensor, food samples (milk, rice, oats, and corn) fortified with different AFB_1 concentrations were analyzed by the established sensor. As shown in Table 1, the detected concentrations for each sample were consistent with the spiked concentrations. The recovery rates of the colorimetric mode and the fluorescent mode were in the range of 91.14%–107.54% with a relative standard deviation RSD < 7.53% and 95.18%–104.76% with a RSD < 7.48%. These results indicated that the proposed dual-mode sensor could be applied for detection AFB_1 in milk, rice, oats, and corn.

4. Discussion

In this study, a colorimetric and fluorescent dual-mode sensor based on Mn_3O_4 NPs nanozyme and PVP-Au/CuNCs for the sensitive, accurate, and rapid determination of AFB_1 was developed. The specific binding of AFB_1 to aptamer regulates the color change of oxTMB by regulating the oxidase-like activity of Mn_3O_4 NPs, achieving the colormetric detection with a good linear range of 0–56 μg/L, a LOD of 0.36 μg/L. The oxTMB effectively quenches the orange fluorescence of PVP-Au/CuNCs *via* IFE or FRET, the relative fluorescence intensity showed a good linear relationship with AFB_1 concentration in the range of 2.86–40.00 μg/L with a LOD of 0.29 μg/L. The dual-mode sensor developed in this study integrates dual-signal, self-calibration, label-free, and high specificity, providing a new insight for the detection of mycotoxins in food.

Declaration of competing interest

The authors declare that they have no known competing financial interests or personal relationships that could have appeared to influence the work reported in this paper.

Data availability

Data will be made available on request.

Acknowledgements

This work was supported by the Scientific Key Project of Hunan Provincial Department of Education (23A0204), Open Project Program of Ministry of Agriculture and Rural Affairs Key Laboratory of Testing and Evaluation for Agro-product Safety and Quality (NK202401) and Dongting Laboratory Special Fund Project (2024-DTPY-008).

Appendix A. Supplementary data

Supplementary data associated with this article can be found, in the online version, at http://doi.org/10.26599/FSHW.2024.9250363.

References

[1] A. Jallow, H. Xie, X. Tang, et al., Worldwide aflatoxin contamination of agricultural products and foods: from occurrence to control, Comp. Rev.

Food Sci. Food Safe. 20 (2021) 2332-2381. https://doi.org/10.1111/1541-4337.12734.

[2] J. Xiong, S. He, L. Qin, et al., Aptasensor-based assay for dual-readout determination of aflatoxin B_1 in corn and wheat *via* an electrostatic force-mediated FRET strategy, Microchim. Acta 190 (2023) 80. https://doi.org/10.1007/s00604-023-05641-1.

[3] P. Chandravarnan, D. Agyei, A. Ali, Green and sustainable technologies for the decontamination of fungi and mycotoxins in rice: a review, Trends Food Sci. Technol. 124 (2022) 278-295. https://doi.org/10.1016/j.tifs.2022.04.020.

[4] N. Xu, Y. Xiao, Q. Xie, et al., Occurrence of aflatoxin B_1 in total mixed rations and aflatoxin M1 in raw and commercial dairy milk in northern China during winter season, Food Control 124 (2021) 107916. https://doi.org/10.1016/j.foodcont.2021.107916.

[5] T. Zhong, S. Li, X. Li, et al, A label-free electrochemical aptasensor based on AuNPs-loaded zeolitic imidazolate framework-8 for sensitive determination of aflatoxin B_1, Food Chem. 384 (2022) 132495. https://doi.org/10.1016/j.foodchem.2022.132495.

[6] N. Wang, C. Duan, X. Geng, et al., One step rapid dispersive liquid-liquid micro-extraction with in-situ derivatization for determination of aflatoxins in vegetable oils based on high performance liquid chromatography fluorescence detection, Food Chem. 287 (2019) 333-337. https://doi.org/10.1016/j.foodchem.2019.02.099.

[7] S. Zhang, S. Zhao, S. Wang, et al., Development of lateral flow immunochromatographic strips for micropollutant screening using colorants of aptamer-functionalized nanogold particles, part II: experimental verification with aflatoxin B_1 and chloramphenicol, J. AOAC Int. 101 (2018) 1408-1414. https://doi.org/10.5740/jaoacint.18-0056.

[8] L. Song, J. Li, H. Li, et al., Highly sensitive SERS detection for aflatoxin B_1 and Ochratoxin A based on aptamer-functionalized photonic crystal microsphere array, Sens. Actuators B: Chem. 364 (2022) 131778. https://doi.org/10.1016/j.snb.2022.131778.

[9] K. Pakshir, Z. Mirshekari, H. Nouraei, et al., Mycotoxins detection and fungal contamination in black and green tea by HPLC-based method, J. Toxicol. 2020 (2020) 1-7. https://doi.org/10.1155/2020/2456210.

[10] H.D. Cho, J.H. Suh, S. Feng, et al., Comprehensive analysis of multi-class mycotoxins in twenty different species of functional and medicinal herbs using liquid chromatography-tandem mass spectrometry, Food Control 96 (2019) 517-526. https://doi.org/10.1016/j.foodcont.2018.10.007.

[11] X. Wu, X. Zhang, Y. Yang, et al., Development of a deep eutectic solvent-based matrix solid phase dispersion methodology for the determination of aflatoxins in crops, Food Chem. 291 (2019) 239-244. https://doi.org/10.1016/j.foodchem.2019.04.030.

[12] Y. Liu, D. Liu, C. Li, et al., Chromatographic methods for rapid aflatoxin B_1 analysis in food: a review, Crit. Rev. Food Sci. Nutr. (2022) 1-18. https://doi.org/10.1080/10408398.2022.2155107.

[13] A. De Girolamo, B. Ciasca, J. Stroka, et al., Performance evaluation of LC-MS/MS methods for multi-mycotoxin determination in maize and wheat by means of international Proficiency Testing, TrAC-Trends Anal. Chem. 86 (2017) 222-234. https://doi.org/10.1016/j.trac.2016.11.005.

[14] C. Damphathik, C. Songsiriritthigul, J. Lerdsri, et al., A novel immunosensor based on cobalt oxide nanocomposite modified single walled carbon nanohorns for the selective detection of aflatoxin B_1, Talanta 258 (2023) 124472. https://doi.org/10.1016/j.talanta.2023.124472.

[15] L. Shang, J. Xu, G.U. Nienhaus, Recent advances in synthesizing metal nanocluster-based nanocomposites for application in sensing, imaging and catalysis, Nano Today 28 (2019) 100767. https://doi.org/10.1016/j.nantod.2019.100767.

[16] S.K. Kailasa, S. Borse, J.R. Koduru, et al., Biomolecules as promising ligands in the synthesis of metal nanoclusters: sensing, bioimaging and catalytic applications, Trends Environ. Anal. Chem. 32 (2021) e00140. https://doi.org/10.1016/j.teac.2021.e00140.

[17] J. Yang, Y. Peng, S. Li, et al., Metal nanocluster-based hybrid nanomaterials: fabrication and application, Coord. Chem. Rev. 456 (2022) 214391. https://doi.org/10.1016/j.ccr.2021.214391.

[18] Z. Wei, Y. Pan, G. Hou, et al., Excellent multiphoton excitation fluorescence with large multiphoton absorption cross sections of arginine-modified gold nanoclusters for bioimaging, ACS Appl. Mater. Interfaces. 14 (2022) 2452-2463. https://doi.org/10.1021/acsami.1c16324.

[19] Y. Shi, J. Ma, A. Feng, et al., Aggregation-induced emission of copper nanoclusters, Aggregate 2 (2021) e112. https://doi.org/10.1002/agt2.112.

[20] J. Tang, C. Liu, C. Zhu, et al., High-nuclearity and thiol protected core-shell $[Cu_{75}(S\text{-}Adm)_{32}]^{2+}$: distorted octahedra fixed to Cu_{15} core *via* strong cuprophilic interactions, Nanoscale 15 (2023) 2843-2848. https://doi.org/10.1039/D2NR05921E.

[21] J. Qiu, Q.N. Nguyen, Z. Lyu, et al., Bimetallic janus nanocrystals: syntheses and applications, Adv. Mater. 34 (2022) 2102591. https://doi.org/10.1002/adma.202102591.

[22] S. Borse, Z.V.P. Murthy, S.K. Kailasa, Synthesis of gold and copper bimetallic nanoclusters with papain for fluorescence detection of cortisone in biological samples, Anal. Bioanal. Chem. 415 (2023) 335-343. https://doi.org/10.1007/s00216-022-04412-w.

[23] Y. Wang, M. Gao, J. Yang, et al., Bimetallic Ag/Au nanoclusters encapsulated in ZIF-8 framework: a novel strategy for ratiometric fluorescence detection of doxycycline in food, Food Chem. 445 (2024) 138738. https://doi.org/10.1016/j.foodchem.2024.138738.

[24] H. He, D.W. Sun, H. Pu, et al., Bridging Fe_3O_4@Au nanoflowers and Au@Ag nanospheres with aptamer for ultrasensitive SERS detection of aflatoxin B_1, Food Chem. 324 (2020) 126832. https://doi.org/10.1016/j.foodchem.2020.126832.

[25] Q. Liu, X. Yan, Q. Lai, et al, Bimetallic gold/silver nanoclusters-gold nanoparticles based fluorescent sensing platform *via* the inner filter effect for hyaluronidase activity detection, Sens. Actuators B: Chem. 282 (2019) 45-51. https://doi.org/10.1016/j.snb.2018.11.040.

[26] Y. Pan, X. Wei, X. Guo, et al., Immunoassay based on Au-Ag bimetallic nanoclusters for colorimetric/fluorescent double biosensing of dicofol, Biosens. Bioelectron. 194 (2021) 113611. https://doi.org/10.1016/j.bios.2021.113611.

[27] Y. Shi, W. Li, X. Feng, et al., Sensing of mercury ions in porphyra by copper@gold nanoclusters based ratiometric fluorescent aptasensor, Food Chem. 344 (2021) 128694. https://doi.org/10.1016/j.foodchem.2020.128694.

[28] Y. Huang, J. Ren, X. Qu, Nanozymes: classification, catalytic mechanisms, activity regulation, and applications, Chem. Rev. 119 (2019) 4357-4412. https://doi.org/10.1021/acs.chemrev.8b00672.

[29] X. Liu, Y. Gao, R. Chandrawati, et al., Therapeutic applications of multifunctional nanozymes, Nanoscale 11 (2019) 21046-21060. https://doi.org/10.1039/C9NR06596B.

[30] X. Li, L. Wang, D. Du, et al., Emerging applications of nanozymes in environmental analysis: opportunities and trends, TRAC-Trends Anal. Chem. 120 (2019) 115653. https://doi.org/10.1016/j.trac.2019.115653.

[31] Q. Wang, H. Wei, Z. Zhang, et al., Nanozyme: an emerging alternative to natural enzyme for biosensing and immunoassay, TRAC-Trends Anal. Chem. 105 (2018) 218-224. https://doi.org/10.1016/j.trac.2018.05.012.

[32] N. Singh, M.A. Savanur, S. Srivastava, et al., A redox modulatory Mn_3O_4 nanozyme with multi-enzyme activity provides efficient cytoprotection to human cells in a Parkinson's disease model, Angew. Chem. Int. Ed. 56 (2017) 14267-14271. https://doi.org/10.1002/anie.201708573.

[33] J. Yao, Y. Cheng, M. Zhou, et al., ROS scavenging Mn_3O_4 nanozymes for *in vivo* anti-inflammation, Chem. Sci. 9 (2018) 2927-2933. https://doi.org/10.1039/C7SC05476A.

[34] S. Liu, M. Wang, H. Deng, et al., A colorimetric and phosphorescent dual-mode nanosensing platform for the sensitive detection of tobramycin in dairy products, Food Biosci. 57 (2024) 103589. https://doi.org/10.1016/j.fbio.2024.103589.

[35] M.S. Hizir, M. Top, M. Balcioglu, et al., Multiplexed activity of perAuxidase: DNA-capped AuNPs act as adjustable peroxidase, Anal. Chem. 88 (2016) 600-605. https://doi.org/10.1021/acs.analchem.5b03926.

[36] Y. Yang, Y. Yin, X. Li, et al., Development of a chimeric aptamer and an AuNPs aptasensor for highly sensitive and specific identification of aflatoxin B_1, Sens. Actuators B: Chem. 319 (2020) 128250. https://doi.org/10.1016/j.snb.2020.128250.

[37] G.B. Asl, M. Arvand, M.F. Habibi, High affinity aptamers for ultra-sensitive detection of aflatoxin B_1 in milk and groundnut samples with label-free photo-electrochemical aptasensor, Food Chem. 397 (2022) 133829. https://doi.org/10.1016/j.foodchem.2022.133829.

[38] X. Hu, H. Cao, W. Dong, et al., Ratiometric fluorescent sensing of ethanol based on copper nanoclusters with tunable dual emission, Talanta 233 (2021) 122480. https://doi.org/10.1016/j.talanta.2021.122480.

[39] J. Wang, H. Tao, T. Lu, et al., Adsorption enhanced the oxidase-mimicking catalytic activity of octahedral-shape Mn_3O_4 nanoparticles as a novel colorimetric chemosensor for ultrasensitive and selective detection of arsenic, J. Colloid Interface Sci. 584 (2021) 114-124. https://doi.org/10.1016/j.jcis.2020.09.107.

[40] J. Xiong, S. He, S. Zhang, et al., A label-free aptasensor for dual-mode detection of aflatoxin B_1 based on inner filter effect using silver nanoparticles and arginine-modified gold nanoclusters, Food Control 144 (2023) 109397. https://doi.org/10.1016/j.foodcont.2022.109397.

[41] S. Li, F. Wang, B. Zhao, et al., MnO_2 nanoflowers based colorimetric and fluorescent dual-mode aptasensor for sensitive detection of aflatoxin B_1 in milk, Anal. Chim. Acta. 1279 (2023) 341844. https://doi.org/10.1016/j.aca.2023.341844.

[42] X. Hu, W. Wang, Y. Huang, Copper nanocluster-based fluorescent probe for sensitive and selective detection of Hg^{2+} in water and food stuff, Talanta 154 (2016) 409-415. https://doi.org/10.1016/j.talanta.2016.03.095.

[43] Y. Yang, A. Han, R. Li, et al., Synthesis of highly fluorescent gold nanoclusters and their use in sensitive analysis of metal ions, Analyst 142 (2017) 4486-4493. https://doi.org/10.1039/C7AN01348E.

[44] Y. Li, H. Tan, X.Y. Yang, et al., Well shaped Mn_3O_4 Nano-octahedra with anomalous magnetic behavior and enhanced photodecomposition properties, Small 7 (2011) 475-483. https://doi.org/10.1002/smll.201001403.

[45] J. Wang, Y. Wu, P. Zhou, et al., A novel fluorescent aptasensor for ultrasensitive and selective detection of acetamiprid pesticide based on the inner filter effect between gold nanoparticles and carbon dots, Analyst 143 (2018) 5151-5160. https://doi.org/10.1039/C8AN01166D.

[46] Y.S. Alqahtani, A.M. Mahmoud, M.M. El-Wekil, Bifunctional nanoprobe for dual-mode detection based on blue emissive iron and nitrogen co-doped carbon dots as a peroxidase-mimic platform, Talanta 253 (2023) 124024. https://doi.org/10.1016/j.talanta.2022.124024.